www.acsabm.org

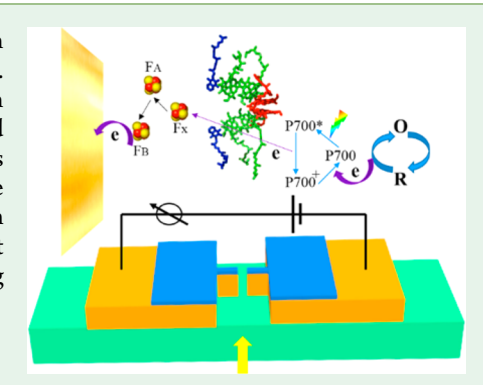
Plasmon-Exciton Coupling in Photosystem I Based Biohybrid **Photoelectrochemical Cells**

Zheng Zeng, Taylor Mabe, Wendi Zhang, Bhawna Bagra, Zuowei Ji, Ziyu Yin, Kokougan Allado, and Jianjun Wei*

Department of Nanoscience, Joint School of Nanoscience and Nanoengineering, University of North Carolina at Greensboro, Greensboro, North Carolina 27401, United States

Supporting Information

ABSTRACT: The light-induced property of photosystem I (PSI) has been utilized to convert solar energy to electrical energy in photoelectrochemical cells. Here we provide new results on the relationship between surface plasmon generation (SPG) efficiency of nanoslits and the experimentally obtained photocurrent by immobilizing PSI on the gold nanoslit electrode surfaces regarding different nanoslit widths. The photocurrent increases with the increment of SPG efficiency. This finding can be attributed to the phenomenon of plasmon-exciton coupling effect on the PSI in the nanoslits. The enhancement of photocurrent generation is discussed on the basis of plasmonic light trapping and plasmon-induced resonance energy transfer.



KEYWORDS: photosystem I, surface plasmon resonance, plasmon-exciton coupling, photocurrent, photoelectrochemistry

■ INTRODUCTION

Because of the photoelectric effect first discovered in 1839, photosystem I (PSI, ~500 kDa protein supercomplex) has been widely used to efficiently capture sunlight for achieving efficient biohybrid photoenergy conversion devices. 1-3 In the photosynthesis process, photoexcited electrons are transported at a 1 µs time scale across the thylakoid membrane by using PSI as a photodiode at a quantum efficiency closing to 100%.⁴ Within PSI, through an internal electron-transfer chain including chlorophylls, phylloquinones, and iron-sulfur cluster, the electron transfer happens between the photoexciting P700 reaction center and iron-sulfur clusters terminating at the F_B cluster.^{6,7} On the basis of the rapid electron transfer and high energy conversion efficiency of PSI, Greenbaum first photoreduced platinum upon the chloroplast's surface by using the reducing power of PSI.8 Then Gerster successfully measured the photocurrent using a single PSI and obtained a photocurrent of 10 pA by a near-field scanning optical microscopy.9 By electrochemically integrating an electrode with PSI, Baldo developed a photovoltaic device (solid-state) by employing PSI as the active species. 10 On the basis of molecular wires on the gold electrode, a current density was obtained to be 88 nA/cm², achieving an enhancement factor of 2.2 over that of the earlier reported system. 11,12 Moreover, the electrode with a nanostructured gold layer has been conducted to act as a positive factor by increasing the photocurrent of PSI. 13,14 Over the past decade, to improve biohybrid devices, much research has been conducted to electrochemically integrate an electrode with PSI via creating covalent attachments, 15 increasing surface area, 16 improving cell design, 17 increasing film thickness, 18 and applying semiconducting electrode, ¹⁹ etc.

Conforming to these reports, light-harvesting enhancement has been considered to be one of the critical factors to design a biohybrid photoelectrochemical cell.²⁰ To improve the coupling efficiency of plasmonic resonance and active species in biomaterial based systems, the strategies based on the plasmon-induced resonance energy transfer (PIRET)^{21,22} and metal particle-enhanced light emission have been developed.^{23,24} Recently, to increase the light absorption and photocurrent generation of PSI, surface plasmon enhancement related coupling of plasmonic resonance and active species was used focusing on the localized surface plasmon resonance (LSPR) by improving the photoactivity of PSI with the gold nanoparticles due to confined collective electronic oscillations. 25-29 This is because that the properties of PSI could be tuned by the enhanced fields derived from the spatially confined LSPR corresponding to the optical excitation at or near the resonant energies. Generally, LSPR and surface plasmon polariton (SPP) are two distinct forms of surface plasmon resonance. According to the origin of SPP, visible or near-infrared frequency electromagnetic waves occur at the interface of metal—dielectric materials.^{30,31} To date, rare reports focus on the SPP effect on PSI and the metallic nanostructure in combination with PSI for implementation of its photoelectric functionality at the nanoscale, especially the

Received: June 20, 2018 Accepted: August 14, 2018 Published: August 15, 2018



ACS Applied Bio Materials Article

fundamental relationship between the photocurrent generation and the surface plasmon generation (SPG) efficiency. Here the SPG efficiency is a term used to quantitatively describe how the surface waves scatter, launch, and propagate at the nanostructure interface by matching the continuous electromagnetic field quantities.^{30,31}

In this work, we used a nanoslit design for an electrochemical setup and, for the first time, observed the photocurrent generation of PSI proteins in a nanoscale plasmonic structure. The PSI was extracted from spinach (Figure S1) with featured absorbance peaks at both 435 and 670 nm (Figure S2).³² The PSI proteins were immobilized at a nanoplasmonic electrochemical device for photocurrent measurements with light excitation. Each device was milled to have one slit of the width at 50, 100, 200, 300, or 400 nm at the bridge center (Figures S3-S6). The present work considered using a semianalytical SPG model and numerical simulations to demonstrate that the nanoslit width could induce changes in the photocurrent generation from the PSI proteins due to different SPG efficiencies. The results may offer new information to study the photovoltaic enhancement of PSI and give hints to develop an artificial light-harvesting

MATERIALS AND METHODS

PSI Preparation. Spinach leaves were purchased from a supermarket and used for the PSI extraction and purification. The steps of the extraction of thylakoid membranes from the spinach leaves and the isolation and purification of PSI complexes from the thylakoids via the methods of Ciesielski.⁶

Fabrication of Nanoplasmonic Electrochemical Devices. We used AutoCAD to draw the sketch of a dark-field photomask and then used a high-resolution printer (25400 DPI) to print it on the transparency film. The design of the photomask is shown in Figure S3. Glass slides (Globe diamond white) were used as substrates and were cleaned in a piranha bath (3:1 H₂SO₄/H₂O₂), rinsed with DI water, dried with a nitrogen stream, and cleaned in an oxygen plasma (200 W, 2 min). After that, we used the hot plate to dehydrate the substrates at 180 °C. A negative photoresist (JSR NFR 016 D2) was spin applied to the glass slides to a thickness of 3.5 μ m, exposed, and developed. In contrast to the supplied data sheet, a substrate-priming step was omitted and an O2 plasma descum was added. Microscopy images and profilometry plots were obtained after each process step. Metal deposition was performed by evaporation (Kurt Lesker PVD75 e-beam evaporator). After a base pressure of 1.0×10^{-6} Torr was reached, Ti was evaporated at a rate of 0.5 Å/s to a thickness of 4.6 nm, Au was evaporated at a rate of 4.4 Å/s to a thickness of 226.3 nm, and then Ti was evaporated at a rate of 0.4 Å/s to a thickness of 4.4 nm. SiO₂ was used as a capping layer and 100.1 nm was deposited atop the final Ti layer at a rate of 1.5 Å/s. We used the acetone bath to sonicate for the lift-off process. A positive photoresist (Shipley S1827) was spin coated onto the patterned substrate and exposed through the second photomask. The top oxide layer was dry etched with reactive ion etching (LAM Rainbow 4400) using a mixture of CF₄/O₂. The positive photoresist was stripped and a nanoslit was milled in the center of each substrate with focused ion beam milling (Zeiss Auriga). Each device was milled to have one slit (with a slit width of 50, 100, 200, 300, or 400 nm) at the bridge center (Figure

Immobilization of PSI on Gold Nanoslit Surfaces. The method for protein immobilization has been reported in detail previously. In brief, O_2 plasma (South Bay Technologies PC2000 Plasma Cleaner) was used to clean the gold slide electrode for 3 min. A mixed self-assembled monolayer (SAM) of 11-mercaptoundecanoic acid (Sigma-Aldrich) and 8-mercapto-octanol (Sigma-Aldrich) was formed by incubating in an absolute ethanol solution (ACROS Organics) containing a 1:2 mol ratio of the two alkanethiols for 2

days. The SAM was activated by a 10 mM PBS solution with 0.5 mM EDC/NHS (Sigma-Aldrich) for 2 h. After rinsing with a 10 mM PBS solution, the PSI was immobilized to the gold surfaces via incubating in a 10 mM PBS solution with $\sim\!\!1$ mM PSI for 2 h.

Electrochemical Measurement. Chronoamperometry (CA) photocurrent measurements were conducted using an electrochemical workstation (VMP3, BioLogic Instrument) with both sides of the gold slide as a testing system under a 0.2 V applied voltage in a homemade Faraday cage by the aluminum foil. Figure S6 shows the electrochemical device slide. A bridge center was fully covered by the electrolyte solution containing 20 mM methylene blue (MB) redoxactive mediator with 100 mM KCl in 10 mM PBS solution. We then used the copper tape piece to electrically connect either side of the electrode. The photoinduced measurement was carried out using the LS-1 white light source with a tungsten halogen lamp (Ocean Optics Inc.) connected with an optical fiber and the area for the nanoslit region was fully illuminated by the light source. Note that the external conditions include the light excitation (without/with light) for different testing systems (SAM/gold slide without PSI immobilization and SAM/gold slide with PSI immobilization).

Semianalytical Analysis. With a semianalytical model, ^{30,31} the SPG efficiency, *e*, at the Au–glass interface of the nanoslit can be calculated as follows:

$$e = |\alpha^{+}(w/2)|^{2} = |\alpha^{-}(w/2)|^{2} = \frac{4w'n_{1}^{3}}{\pi n_{2}^{2}} \left| \frac{\varepsilon^{1/2}}{\varepsilon + n_{1}^{2}} \right| \left| \frac{I_{1}}{1 + (n_{1}/n_{2})w'I_{0}} \right|^{2}$$
(1)

which correlates to the SPG coefficient (α) , nanoslit width (w), scaled width (w'), refractive index (n), dielectric constant (ε) , and integration number (I) (see details in Supporting Information).

Finite-Difference Time-Domain (FDTD) Simulations. The electric or magnetic field intensity profiles of the nanoslit were calculated by a Lumerical FDTD method. 31,34 Considering the background of air, the refractive index was assumed to be 1.0 in the total mesh area. Perfectly matched layer (PML) was applied for the boundary conditions. The indices of Au and glass were obtained from the data of optical constants of solids. Electric—magnetic field distribution calculations were performed at different slit width. Using the Drude-Lorentz model, the transverse electric/magnetic (TE/TM) equations were obtained by a Fourier transform of the polarization. 35

■ RESULTS AND DISCUSSION

We first study the photoelectric response of immobilized PSI on the gold slide electrodes through the mixed SAM (Figure 1). This strategy of covalent binding to the protein's amino groups for immobilization may decrease PSI large-conformational motion.^{3,36} The action spectrum of the PSI immobilized inside the nanoslit surfaces (Figure S7) was obtained by measuring the photocurrent in a 20 mM MB redox-active mediator (with -0.2 V vs Ag/AgCl formal potential) associated with 100 mM KCl in 10 mM PBS under light irradiation using the LS-1 white light source. Similar to the relaxation pathways that occur in the interface of a semiconductor and an electrolyte, electron-hole pairs (e⁻-h⁺) can undertake different pathways, which include electron transfer to redox species, electron transfer to the substrate, and electron—hole pair radiative recombination. 37,38 In this case, under light illumination of the PSI, an oxidized P700+ donor site and a reduced F_B acceptor can be generated by the photoninduced electron-hole pairs separation. Consequently, a direct electron transfer would occur according to the following details. After photoexciting P700 center, the F_B end will accept an electron from the photoexcited P700 center through an internal electron-transfer chain, and then transfer it to the gold electrode. Gold electrode is an electron acceptor compatible with the F_B cluster in PSI, leading to an increased electrode ACS Applied Bio Materials Article

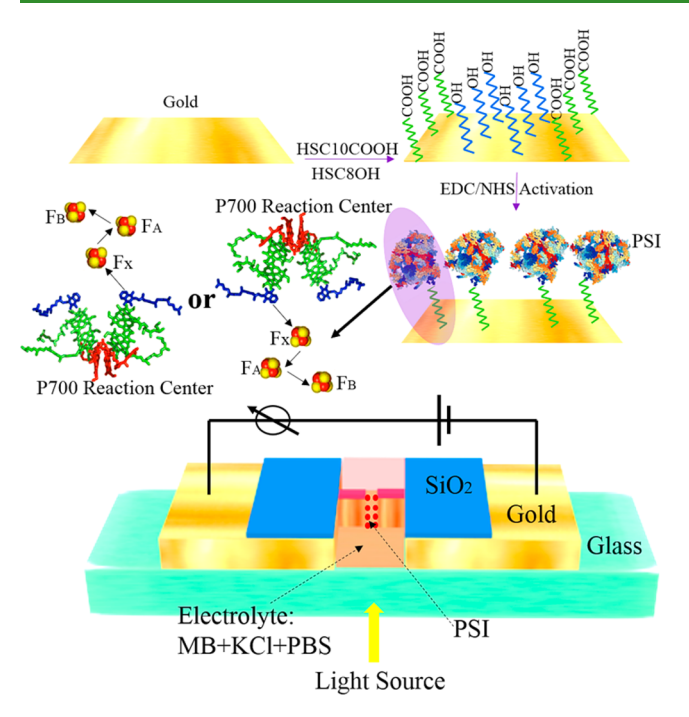


Figure 1. Schematic view of a method for the PSI immobilization with a SAM and a setup for the light associated electrochemistry analysis of PSI.

current. Meanwhile, before another photon can re-excite P700 center in the PSI, the oxidized P700⁺ center must be reduced by reaccepting a new electron. In our system, the MB in solution acts as electron donors to the oxidized P700⁺ center (Figure 2a). Atomic coordinates from PDB entry 2O01 are used to make the structure of PSI.³⁹

Figure 2b-f show histogram distributions of photocurrent generation by the immobilized PSI at an applied voltage of 0.2 V in nanoslits. Figures S7 and S8 show the representative CA measurements of nanoslit electrodes with or without immobilized PSI, respectively. In the CA measurements, the potential of the working electrode is stepped and recorded after 10 s of waiting time from the initial to the steady-state current. The photocurrent was recorded as a function of time from the photoexciting processes occurring at the side of nanoslit. The highest photocurrent (avg. ~181 nA by a 100 nm nanoslit width device) and the lowest (avg. ~76 nA by a 400 nm nanoslit width device) were obtained. Since the untreated gold nanoslits for all different widths have no obvious photocurrent generation under the light irradiation, we conclude that the photocurrent is originated from the PSI immobilized at the gold electrode surfaces due to the photoelectric effect. In accordance with a reported PSIIbased photoelectrochemical cell,⁴⁰ the current-voltage curve (Figure S9) of the electrochemical cell with PSI immobilization (using nanoslit width of 100 nm) also supports the photoactive role of PSI in photocurrent generation. Considering that PSI proteins should have either the acceptor side (F_B) or the donor side (P700) in contact with the SAM-gold electrode to undergo a redox reaction, 3,7 the average value of the net photocurrent was obtained from 15 measurements (chosen from 18 measurements including 2 nanoslit devices with the same naonoslit width × self-assembly performed on the same device 3 times × measurements 3 times) for each nanoslit width device (Table S1). Note that three trials were

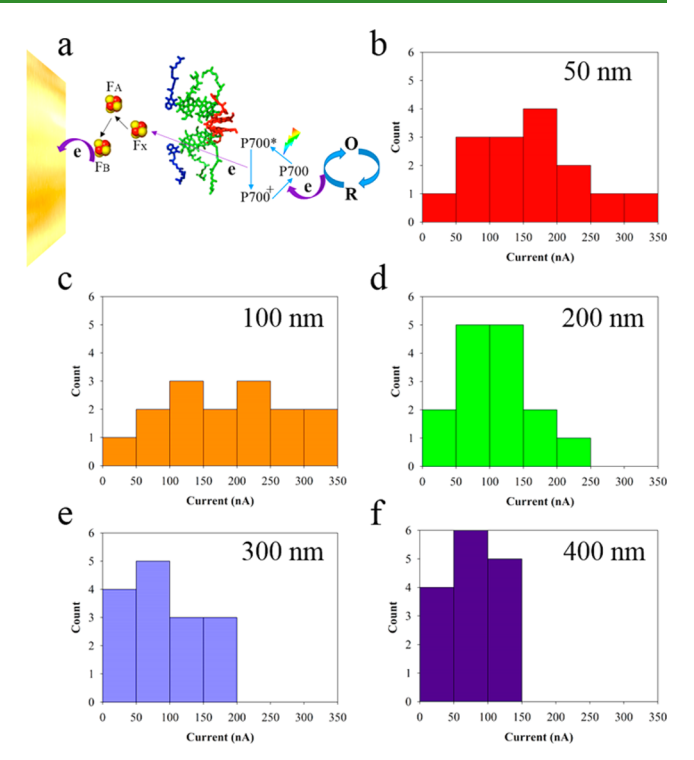


Figure 2. (a) Illustration of the electron transfer from PSI to Au slide electrode with the reaction-center electron transfer chain. (b-f) Photocurrent generation analysis and histograms for the electrochemical devices with different nanoslit widths.

failed (no photocurrent measured) possibly because of the release of chlorophyll or denature of PSI with the light irradiation. By using the excitation area of gold electrode about $18.2~\mu\text{m}^2$ (fabrication information) with immobilized PSI, in our nanoscale device, the current density could be roughly obtained to be about $9.95~\text{nA}/\mu\text{m}^2$ for the 100 nm width nanoslit device. Considering that, in the centimeter-scale biohybrid photoelectrochemical cells, the photocurrent generation of PSI films on p-doped silicon can be obtained to be about $875~\mu\text{A/cm}^2$, our results may suggest the good integration of photocurrent magnitude of 10 pA created by a single PSI using such a nanoscale energy conversion device.

Next, we move to study the relationship of SPG efficiencies with the nanoslit width and incident light wavelengths. Regarding the bounded SPP modes with the geometric diffraction presenting on the interface of a gold surface and a glass one, the SPP scattering coefficients and efficiencies at the slit apertures are calculated. The scheme in Figure 3a depicts the key parameters for the SPG calculation with respect to the geometry of the nanoslit and property of light source (a normally incident plane wave), including the slit width of w, the SPG coefficients at the Au-glass interface in an inverse direction (α^+ and α^-), the refractive index of glass ($n_{\rm glass}$ of 1.41), and that inside the slits ($n_{\rm air}$ of 1). The SPG efficiency on one side of the aperture was obtained using the eq 1.

After a numerical calculation by a Python script (Table S2) and an analytical technique, for one side of the nanoslit structure, the SPG efficiency e can be obtained.³⁴ As shown in Figure 3b, with the increase of light wavelength (λ from 600 to 1200 nm) and scaled slit width (w' from 0.1 to 1.0), the SPG efficiencies were demonstrated dependence as a function of λ and w'. The SPG efficiency is higher in the visible frequency region than that in the near-infrared region because of the

ACS Applied Bio Materials

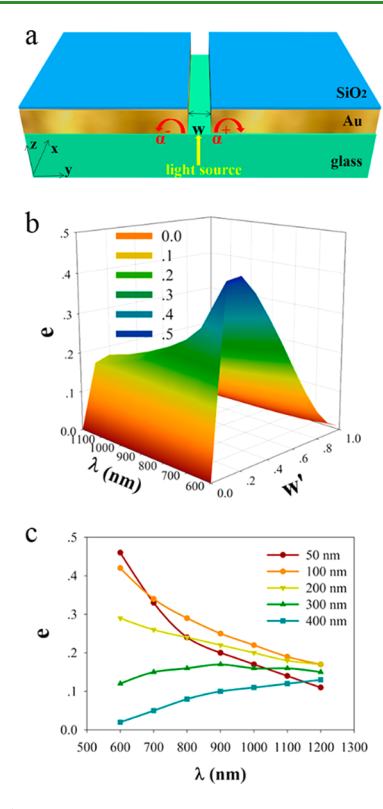


Figure 3. (a) Illustration of the key parameters for the SPG calculation with respect to the structure of the nanoslit and light source. (b) Plot of SPG efficiencies e at the Au–glass interface with respect to λ and w'. (c) Relationship of SPG efficiencies e at the Au–glass interface with λ at different w.

stronger visible frequency electromagnetic waves occurring at the Au–glass interface. Considering that the optimal slit width is related to the optimal scaled slit width, a value of w'=0.26 is obtained to estimate the optimal slit width. For example, the optimal widths are $w=0.18\lambda$ for the nanoslit with refractive index of 1.41. Moreover, according to different values for w and λ , one can get different e values (Figure 3c, Table S3) and average SPG efficiencies (Table S1).

The electromagnetic field distribution of the nanoslit structure (without PSI immobilization) was further modeled via a FDTD method (Figure S10). A Fourier transform polarization was initiated and implementing it into the FDTD formalism resulted in the TE/TM equations. The electromagnetic (EM) field distribution indicates the plasmonic intensity at the Au-glass interface with the strength of EM₁₀₀ > $EM_{50} > EM_{200} > EM_{300} > EM_{400}$, which is consistent with the results of the nanoslit structure with PSI immobilization (Figure S11). It is interesting to compare the FDTD result with PSI immobilization to that without PSI with the same nanoslit width. Addition of a biolayer on the side of nanoslit decreases the plasmonic intensity due to the increase of refractive index. Note that the refractive index and thickness of the PSI film were estimated to be 1.5 and 10 nm, 41,42 respectively. The FDTD simulation agrees well with the semianalytical model results for SPG efficiencies from the five nanoslit devices. Hence, the stronger charge oscillation induced by the improved SPP excitation results in an enhanced EM field at the Au-glass interface. 43,44

Additionally, we used the CytoViva Hyperspectral imaging system to measure the light intensity in the nanoslit (Figure 4). The ENVI software was used to get the light intensity data in

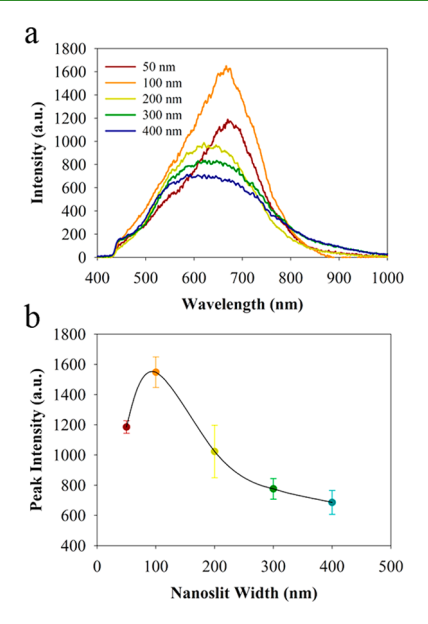


Figure 4. (a) Light intensity measurements for different nanoslit structures in reflection mode. (b) Peak intensity versus different nanoslit structures.

the center of the nanoslit by taking the image pixel by pixel. Spectra can be obtained from point to point and it gives the option to take the average spectra. We took the average spectra of each nanoslit three times to check the consistency and accuracy. The light intensity data are well consistent with the SPG efficiency of the electrochemical devices. More importantly, one absorbance peak wavelength of PSI (670 nm) locates within the range of light intensity peak wavelength (600–700 nm). These results suggest that the plasmon-induced light trapping provides insight into the SPG efficiencies corresponding to the EM field distributions.

Figure 5 shows the photocurrent generation and SPG efficiency for the nanoslit electrochemical devices (D) as a

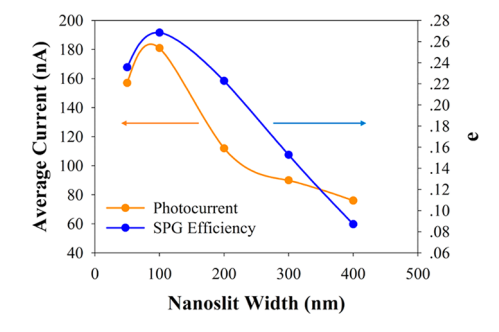


Figure 5. Plot of average photocurrent in experimental measurements or calculated SPG efficiency versus nanoslit width.

function of nanoslit width. They both have the same order of $D_{100} > D_{50} > D_{200} > D_{300} > D_{400}$. Regarding the plasmonic effects on the metal—semiconductor photoelectrochemical cells, ⁴⁵ light trapping/scattering, direct electron transfer (hot electron injection), and PIRET have been recognized as three major mechanisms. ⁴⁶ In this study, the photocurrent originated from the electron transfer from immobilized PSI to the gold electrode, and the light intensity spectra in the nanoslits presented an overlap with the absorption peak of PSI. Hence, for this hybrid metal—biology system, it is expected that the plasmonic light trapping excitation and the PIRET between

ACS Applied Bio Materials

gold and PSI should play major roles in the enhanced photocurrent generation. Specifically, larger SPG efficiency (also called larger collective electron oscillations or larger electromagnetic near-field propagation) can concentrate more incident energy due to the larger combined dipole moment generation. This concentrated incident energy can be nonradiatively transferred to the PSI proteins though PIRET to generate more electron-hole pairs in PSI, 47,48 resulting in more excited electrons inside the P700 center, thus more available P700+ donor sites and F_B acceptor sites for better efficient electron exchange in PSI. As a result, more electrons from the F_B end transfer to the gold electrode, leading to an increased photocurrent. Meanwhile, since plasmon resonance induced electron-hole separation potentially makes the kinetics of electron transfer faster, the gold electrode will receive more electrons under a unit time scale. Hence, the net photocurrent generation of the PSI is well consistent with the SPG efficiency of the electrochemical devices (Figure 5) with nanoslit width dependence and maximized at 100 nm slit in this work.

CONCLUSIONS

This work demonstrates how surface plasmon resonance influence the photocurrent generation from PSI by immobilizing PSI on gold surfaces in a nanoslit. The energy conversion (photocurrent) is greatly enhanced, which is correlated to the SPG efficiency and EM field enhancement in the nanoslit. The results could be attributed to the phenomenon of plasmon–exciton coupling with the effects of plasmon-induced energy transfer and light trapping. This study offers promise to develop a novel photosystem I based biohybrid photoelectrochemical cell for high efficiency energy conversion.

ASSOCIATED CONTENT

S Supporting Information

The Supporting Information is available free of charge on the ACS Publications website at DOI: 10.1021/acsabm.8b00249.

PSI characterization; electrochemical device fabrication and characterization; photocurrent measurements; surface plasmon generation efficiency calculation; model for SPG calculation, FDTD simulation (PDF)

AUTHOR INFORMATION

Corresponding Author

*E-mail: j_wei@uncg.edu. Phone: 1-336-285-2859.

ORCID ®

Jianjun Wei: 0000-0002-2658-0248

Notes

The authors declare no competing financial interest.

ACKNOWLEDGMENTS

This work is partially supported by US NSF (No. 1511194) and NC state fund through Joint School of Nanoscience and Nanoengineering (JSNN), UNCG. This work was performed at the JSNN, a member of South Eastern Nanotechnology Infrastructure Corridor (SENIC) and National Nanotechnology Coordinated Infrastructure (NNCI), which is supported by the National Science Foundation (ECCS-1542174).

REFERENCES

- (1) Paul, S.; Neese, F.; Pantazis, D. A. Structural Models of The Biological Oxygen-Evolving Complex: Achievements, Insights, and Challenges for Biomimicry. *Green Chem.* **2017**, *19*, 2309–2325.
- (2) Gizzie, E. A.; LeBlanc, G.; Jennings, G. K.; Cliffel, D. E. Electrochemical Preparation of Photosystem I–Polyaniline Composite Films for Biohybrid Solar Energy Conversion. *ACS Appl. Mater. Interfaces* **2015**, *7*, 9328–9335.
- (3) LeBlanc, G.; Gizzie, E.; Yang, S.; Cliffel, D. E.; Jennings, G. K. Photosystem I Protein Films at Electrode Surfaces for Solar Energy Conversion. *Langmuir* **2014**, *30*, 10990–11001.
- (4) Nelson, N. Plant Photosystem I The Most Efficient Nano-Photochemical Machine. *J. Nanosci. Nanotechnol.* **2009**, *9*, 1709–1713.
- (5) Brettel, K.; Leibl, W. Electron Transfer in Photosystem I. Biochim. Biophys. Acta, Bioenerg. 2001, 1507, 100-114.
- (6) Ciesielski, P. N.; Hijazi, F. M.; Scott, A. M.; Faulkner, C. J.; Beard, L.; Emmett, K.; Rosenthal, S. J.; Cliffel, D.; Kane Jennings, G. Photosystem I Based Biohybrid Photoelectrochemical Cells. *Bioresour. Technol.* **2010**, *101*, 3047–3053.
- (7) Ciobanu, M.; Kincaid, H. A.; Lo, V.; Dukes, A. D.; Kane Jennings, G.; Cliffel, D. E. Electrochemistry and Photoelectrochemistry of Photosystem I Adsorbed on Hydroxyl-Terminated Monolayers. *J. Electroanal. Chem.* **2007**, *599*, 72–78.
- (8) Greenbaum, E. Platinized Chloroplasts: A Novel Photocatalytic Material. *Science* **1985**, 230, 1373–1375.
- (9) Gerster, D.; Reichert, J.; Bi, H.; Barth, J. V.; Kaniber, S. M.; Holleitner, A. W.; Visoly-Fisher, I.; Sergani, S.; Carmeli, I. Photocurrent of a Single Photosynthetic Protein. *Nat. Nanotechnol.* **2012**, *7*, 673–676.
- (10) Das, R.; Kiley, P. J.; Segal, M.; Norville, J.; Yu, A. A.; Wang, L.; Trammell, S. A.; Reddick, L. E.; Kumar, R.; Stellacci, F.; Lebedev, N.; Schnur, J.; Bruce, B. D.; Zhang, S.; Baldo, M. Integration of Photosynthetic Protein Molecular Complexes in Solid-State Electronic Devices. *Nano Lett.* **2004**, *4*, 1079–1083.
- (11) Terasaki, N.; Yamamoto, N.; Hiraga, T.; Yamanoi, Y.; Yonezawa, T.; Nishihara, H.; Ohmori, T.; Sakai, M.; Fujii, M.; Tohri, A.; Iwai, M.; Inoue, Y.; Yoneyama, S.; Minakata, M.; Enami, I. Plugging a Molecular Wire into Photosystem I: Reconstitution of the Photoelectric Conversion System on a Gold Electrode. *Angew. Chem., Int. Ed.* **2009**, *48*, 1585–1587.
- (12) Yamanoi, Y.; Terasaki, N.; Miyachi, M.; Inoue, Y.; Nishihara, H. Enhanced Photocurrent Production by Photosystem I with Modified Viologen Derivatives. *Thin Solid Films* **2012**, *520*, 5123–5127
- (13) Terasaki, N.; Yamamoto, N.; Hiraga, T. Photo-sensor with Photo-electric Conversion Molecules and a Modified Gold Nanostructured FET Gate Film. *Thin Solid Films* **2009**, *518*, 656–660.
- (14) Terasaki, N.; Yamamoto, N.; Hattori, M.; Tanigaki, N.; Hiraga, T.; Ito, K.; Konno, M.; Iwai, M.; Inoue, Y.; Uno, S.; Nakazato, K. Photosensor Based on an FET Utilizing a Biocomponent of Photosystem I for Use in Imaging Devices. *Langmuir* **2009**, 25, 11969–74.
- (15) Faulkner, C. J.; Lees, S.; Ciesielski, P. N.; Cliffel, D. E.; Jennings, G. K. Rapid Assembly of Photosystem I Monolayers on Gold Electrodes. *Langmuir* **2008**, *24*, 8409–8412.
- (16) Ciesielski, P. N.; Scott, A. M.; Faulkner, C. J.; Berron, B. J.; Cliffel, D. E.; Jennings, G. K. Functionalized Nanoporous Gold Leaf Electrode Films for the Immobilization of Photosystem I. *ACS Nano* **2008**, *2*, 2465–2472.
- (17) Kothe, T.; Pöller, S.; Zhao, F.; Fortgang, P.; Rögner, M.; Schuhmann, W.; Plumeré, N. Engineered Electron Transfer Chain in Photosystem 1 Based Photocathodes Outperforms Electron Transfer Rates in Natural Photosynthesis. *Chem. Eur. J.* **2014**, *20*, 11029–11034
- (18) Ciesielski, P. N.; Faulkner, C. J.; Irwin, M. T.; Gregory, J. M.; Tolk, N. H.; Cliffel, D. E.; Jennings, G. K. Enhanced Photocurrent Production by Photosystem I Multilayer Assemblies. *Adv. Funct. Mater.* **2010**, 20, 4048–4054.

ACS Applied Bio Materials

- (19) LeBlanc, G.; Chen, G.; Gizzie, E. A.; Jennings, G. K.; Cliffel, D. E. Enhanced Photocurrents of Photosystem I Films on p-Doped Silicon. *Adv. Mater.* **2012**, *24*, 5959–5962.
- (20) Kim, I.; Bender, S. L.; Hranisavljevic, J.; Utschig, L. M.; Huang, L.; Wiederrecht, G. P.; Tiede, D. M. Metal Nanoparticle Plasmon-Enhanced Light-Harvesting in a Photosystem I Thin Film. *Nano Lett.* **2011**, *11*, 3091–3098.
- (21) Cushing, S. K.; Li, J.; Meng, F.; Senty, T. R.; Suri, S.; Zhi, M.; Li, M.; Bristow, A. D.; Wu, N. Photocatalytic Activity Enhanced by Plasmonic Resonant Energy Transfer from Metal to Semiconductor. *J. Am. Chem. Soc.* **2012**, *134*, 15033–15041.
- (22) Li, J.; Cushing, S. K.; Meng, F.; Senty, T. R.; Bristow, A. D.; Wu, N. Plasmon-Induced Resonance Energy Transfer for Solar Energy Conversion. *Nat. Photonics* **2015**, *9*, 601.
- (23) Kinkhabwala, A.; Yu, Z.; Fan, S.; Avlasevich, Y.; Müllen, K.; Moerner, W. E. Large Single-Molecule Fluorescence Enhancements Produced by A Bowtie Nanoantenna. *Nat. Photonics* **2009**, *3*, 654–657
- (24) Bardhan, R.; Grady, N. K.; Cole, J. R.; Joshi, A.; Halas, N. J. Fluorescence Enhancement by Au Nanostructures: Nanoshells and Nanorods. *ACS Nano* **2009**, *3*, 744–752.
- (25) Carmeli, I.; Lieberman, I.; Kraversky, L.; Fan, Z.; Govorov, A. O.; Markovich, G.; Richter, S. Broad Band Enhancement of Light Absorption in Photosystem I by Metal Nanoparticle Antennas. *Nano Lett.* **2010**, *10*, 2069–2074.
- (26) Govorov, A. O.; Carmeli, I. Hybrid Structures Composed of Photosynthetic System and Metal Nanoparticles: Plasmon Enhancement Effect. *Nano Lett.* **2007**, *7*, 620–625.
- (27) Fofang, N. T.; Park, T.-H.; Neumann, O.; Mirin, N. A.; Nordlander, P.; Halas, N. J. Plexcitonic Nanoparticles: Plasmon—Exciton Coupling in Nanoshell—J-Aggregate Complexes. *Nano Lett.* **2008**, *8*, 3481—3487.
- (28) Terasaki, N.; Yamamoto, N.; Hiraga, T.; Sato, I.; Inoue, Y.; Yamada, S. Fabrication of Novel Photosystem I—Gold Nanoparticle Hybrids and Their Photocurrent Enhancement. *Thin Solid Films* **2006**, 499, 153–156.
- (29) Nishijima, Y.; Ueno, K.; Yokota, Y.; Murakoshi, K.; Misawa, H. Plasmon-Assisted Photocurrent Generation from Visible to Near-Infrared Wavelength Using a Au-Nanorods/TiO2 Electrode. *J. Phys. Chem. Lett.* **2010**, *1*, 2031–2036.
- (30) Lalanne, P.; Hugonin, J. P.; Rodier, J. C. Theory of Surface Plasmon Generation at Nanoslit Apertures. *Phys. Rev. Lett.* **2005**, *95*, 263902.
- (31) Zeng, Z.; Mendis, M. N.; Waldeck, D. H.; Wei, J. A Semi-Analytical Decomposition Analysis of Surface Plasmon Generation and The Optimal Nanoledge Plasmonic Device. *RSC Adv.* **2016**, *6*, 17196–17203.
- (32) Tian, L.; Xu, P.; Chukhutsina, V. U.; Holzwarth, A. R.; Croce, R. Zeaxanthin-dependent Nonphotochemical Quenching Does Not Occur in Photosystem I in the Higher Plant Arabidopsis Thaliana. *Proc. Natl. Acad. Sci. U. S. A.* **2017**, *114*, 4828.
- (33) Zeng, Z.; Wei, J.; Liu, Y.; Zhang, W.; Mabe, T. Magneto-reception of Photoactivated Cryptochrome 1 in Electrochemistry and Electron Transfer. ACS Omega 2018, 3, 4752–4759.
- (34) Zeng, Z.; Shi, X.; Mabe, T.; Christie, S.; Gilmore, G.; Smith, A. W.; Wei, J. Protein Trapping in Plasmonic Nanoslit and Nanoledge Cavities: The Behavior and Sensing. *Anal. Chem.* **2017**, *89*, 5221–5229.
- (35) Zeng, Z.; Liu, Y.; Wei, J. Recent Advances in Surface-enhanced Raman Spectroscopy (SERS): Finite-difference Time-domain (FDTD) Method for SERS and Sensing Applications. *TrAC, Trends Anal. Chem.* **2016**, *75*, 162–173.
- (36) Wei, J.; Liu, H.; Dick, A. R.; Yamamoto, H.; He, Y.; Waldeck, D. H. Direct Wiring of Cytochrome c's Heme Unit to an Electrode: Electrochemical Studies. *J. Am. Chem. Soc.* **2002**, *124*, 9591–9599.
- (37) Mu, Y. Chemical Functionalization of GaN Monolayer by Adatom Adsorption. J. Phys. Chem. C 2015, 119, 20911–20916.
- (38) Zeng, Z.; Zhang, W.; Arvapalli, D. M.; Bloom, B.; Sheardy, A.; Mabe, T.; Liu, Y.; Ji, Z.; Chevva, H.; Waldeck, D. H.; Wei, J. A

- Fluorescence-Electrochemical Study of Carbon Nanodots (CNDs) in Bio- and Photoelectronic Applications and Energy Gap Investigation. *Phys. Chem. Chem. Phys.* **2017**, *19*, 20101–20109.
- (39) Amunts, A.; Drory, O.; Nelson, N. The Structure of a Plant Photosystem I Supercomplex at 3.4 Å Resolution. *Nature* **2007**, 447, 58–63.
- (40) Yehezkeli, O.; Tel-Vered, R.; Wasserman, J.; Trifonov, A.; Michaeli, D.; Nechushtai, R.; Willner, I. Integrated Photosystem II-Based Photo-Bioelectrochemical Cells. *Nat. Commun.* **2012**, *3*, 742.
- (41) Dunahay, T. G.; Staehelin, L. A. Isolation of Photosystem I Complexes from Octyl Glucoside/Sodium Dodecyl Sulfate Solubilized Spinach Thylakoids. *Plant Physiol.* **1985**, *78*, 606–613.
- (42) Kaye, S.; Zeng, Z.; Sanders, M.; Chittur, K.; Koelle, P. M.; Lindquist, R.; Manne, U.; Lin, Y.; Wei, J. Label-Free Detection of DNA Hybridization with a Compact LSPR-Based Fiber-Optic Sensor. *Analyst* **2017**, *142*, 1974–1981.
- (43) Maier, S. A. Plasmonics: Fundamentals and Applications; Springer, 2007.
- (44) Fort, E.; Gresillon, S. Surface Enhanced Fluorescence. J. Phys. D: Appl. Phys. 2008, 41, 013001.
- (45) Li, J.; Cushing, S. K.; Zheng, P.; Meng, F.; Chu, D.; Wu, N. Plasmon-Induced Photonic and Energy-Transfer Enhancement of Solar Water Splitting by A Hematite Nanorod Array. *Nat. Commun.* **2013**, *4*, 2651.
- (46) Cushing, S. K.; Wu, N. Progress and Perspectives of Plasmon-Enhanced Solar Energy Conversion. *J. Phys. Chem. Lett.* **2016**, *7*, 666–675.
- (47) Koh, A. L.; Fernández-Domínguez, A. I.; McComb, D. W.; Maier, S. A.; Yang, J. K. W. High-Resolution Mapping of Electron-Beam-Excited Plasmon Modes in Lithographically Defined Gold Nanostructures. *Nano Lett.* **2011**, *11*, 1323–1330.
- (48) Wu, N. Plasmonic Metal-Semiconductor Photocatalysts and Photoelectrochemical Cells: A Review. *Nanoscale* **2018**, *10*, 2679–2696.